Colloids and Surfaces A: Physicochem. Eng. Aspects 456 (2014) 273–285

Contents lists available at ScienceDirect

Colloids and Surfaces A: Physicochemical and Engineering Aspects

journal homepage: www.elsevier.com/locate/colsurfa

Effect of relative humidity on the spreading dynamics of sessile drops of blood

W. Bou-Zeid*, D. Brutin

Aix Marseille University, IUSTI UMR 7343, 13013 Marseille, France

HIGHLIGHTS

- Relative humidity change the spreading dynamics.
- Evolution of the wetted area is governed by two distinct regimes.
- Two different spreading exponents are obtained for the two regimes.
- Triple line follows the same behaviour as Tanner's model.

GRAPHICAL ABSTRACT

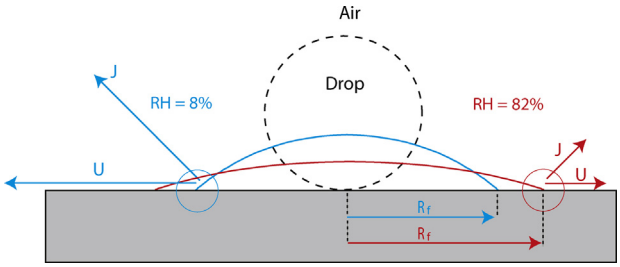

ARTICLE INFO

Article history:
Received 10 March 2014
Received in revised form 28 April 2014
Accepted 2 May 2014
Available online 27 May 2014

Keywords:
Human blood
Biocolloids
Evaporation
Wettability
Adhesion

ABSTRACT

We studied the effect of relative humidity on the initial stages of spreading dynamics for drops of whole human blood. A range of relative humidities from 8% to 90% was studied. Drops of the same volume were gently deposited on ultra-clean microscope glass substrates. We show that the drop spreading is driven by two distinct regimes. The first is characterised by fast dynamics and competition between viscous forces and capillary forces, whereas the second regime is characterised by competition between viscous dissipation and evaporation and exhibits slower dynamics. At early stages of spreading, the power law $r(t) \sim t^n$ ($n = 0.65$) was observed regardless of the humidity. At later stages of spreading, the exponent of the power law $r(t) \sim t^n$ ($n = 0.19$) was found to be higher than that of Tanner's law because of the effect of humidity and Marangoni stresses. Spreading time and spreading dynamics were found to be related to relative humidity. This is explained by the adhesion of red blood cells to the substrate which is similar to the mechanism observed for nanofluid droplets. The mean velocity of the triple line followed the same behaviour as Tanner's model, where the final wetting radius and the apparent contact angle are functions of relative humidity.

1. Introduction

The spreading of liquid drops on solid substrates is a ubiquitous process in nature and is of increasing technological importance. Coffee stain formation, surface spray cooling [1], spray coating [2] and droplet deposition in biomedical applications [3,4] are a few examples in which understanding the fundamentals of spreading dynamics is crucial.

When a liquid droplet contacts a wet solid surface, the unbalanced force (driving forces and braking forces), $\gamma(\cos\theta_e - \cos\theta(U))$ causes the droplet to spread until the contact angle stabilises at the equilibrium angle θ_e, where γ is the liquid–vapour surface tension and $\theta(U)$ the dynamic contact angle at a spreading speed U which is larger than the equilibrium contact angle. The first moments of spreading tend to be rapid (some milli-seconds for millimeter sized water drops) while it takes a much longer time for viscous liquids to completely spread. For a drop of a complete wetting fluid ($\theta_e = 0$)

* Corresponding author. Tel.: +33 491106868; fax: +33 491106969.
E-mail addresses: wassim.bouzeid@etu.univ-amu.fr (W. Bou-Zeid), david.brutin@univ-amu.fr (D. Brutin).

http://dx.doi.org/10.1016/j.colsurfa.2014.05.004
0927-7757/

with radius smaller than the capillary length, $l_c = \sqrt{\gamma/\rho g}$ (effect of gravity is negligible), the drop spreads indefinitely, presumably until it reaches a film thickness controlled by surface forces. The evolution of the wetted surface is reported using either the base spreading radius $r(t)$ or the wetted surface area $A(t) = \pi r^2(t)$.

The hydrodynamic theory emphasises that the initial dynamic wetting is driven by capillary forces and the viscous dissipation of viscous flow within the wedge of liquid near the moving solid/liquid/vapour triple line [5–9]. By balancing surface tension and viscosity, the evolution of the wetted radius of Newtonian fluids, r, was found to scale with time, t, according to Tanner's law: $r(t) \sim R(\gamma t/\mu R)^n$ with $n = 1/10$. This evolution was obtained by assuming that the shape of the drop is a thin spherical cap and that the dynamic contact angle, $\theta(U)$, is related to the dimensionless velocity, Ca, by the Cox–Voinov relation: $\theta(U)^3 \sim Ca$ [5,10]. A small deviation from Tanner's law was reported [11,12] and associated with the non-Newtonian flow properties (shear thinning and normal stresses), in particular, slower spreading kinetics corresponds to an apparent increase in liquid viscosity as the speed of spreading decreases. In order to neglect one of these non-Newtonian flow properties, Rafai et al. [12] studied the spreading in two different dilute or semi-dilute polymer solutions. The flow behaviour of these dilute polymer solutions depends sensitively on the flexibility of the polymer solution [13].

Different power law evolution have been observed for the base radius r depending on wettability, inertia, viscosity and surface tension. However, one of the commonly used methods to analyze spreading is matching the curves of the spreading radius r versus the spreading time t with a power law, $r(t) \sim t^n$, with n being the so-called spreading or wetting exponent. As the radius of the droplet grows beyond the capillary length, the gravity force dominates and the shape of the drop becomes pancake-like, curved only at the drop rim, yielding a spreading exponent $n = 1/8$ when bulk phase fluid dissipation dominates or $n = 1/7$ when contact line fluid dissipation dominates [14].

At the early stage of drop spreading, the power law $r \sim t^{1/2}$ is observed as long as capillarity is balanced by inertia at the contact line. This power law is observed in several experiments and is found to be dependent or independent on surface wettability. Winkels et al. [15] observed a scaling in the contact radius as $r \sim t^{1/2}$ in their experiments involving water drops (low-viscosity, $R = 0.5$ mm) spreading on four different substrates ($\theta_{eq} = 115^\circ$, 100°, 60°, 0°). For their analysis, the contact radius, r, was rescaled with the initial drop radius, R, and time was rescaled with the inertial time scale $\tau = \sqrt{\rho R^3/\gamma}$. Bird et al. [16] stated that the spreading regime is dependent on surface wettability, $r \sim t^n$, where the exponent n depends on the equilibrium contact angle, θ_{eq}. The authors used a timescale of $\sqrt{\rho R^3/\gamma}$ in the inertially dominated regime. Their experiments are performed using droplets of different water–glycerol mixtures on silicon wafer surfaces of varying wettability ($\theta_{eq} = 0^\circ$ to $\theta_{eq} = 180^\circ$). Eddi et al. [17] performed experiments with droplets of different water–glycerin mixtures ($\mu = 115$ mPa s, 50 mPa s, 220 mPa s, 1120 mPa s) on glass substrate. They investigated the effect of initial drop radius, R, the equilibrium contact angle θ_{eq}, and viscosity, μ, on spreading dynamics. They found that the initial stages of spreading are independent of substrate wettability and that the contact radius increases as $r/R \sim (t/\sqrt{\rho R^3/\gamma})^{1/2}$. Carlson et al. [18] investigated the effect of viscosity and wettability on the initial stages of spreading for viscous drops. In this work, the authors observed that the spreading power law grows as $t^{1/2}$ with a dependence on liquid viscosity. The authors concluded that neither inertia nor bulk viscosity are limiting factor in drop spreading but that a specific contact line friction μ_f (independent of drop size) accounts for enhanced dissipation close to the contact line. The authors used a time scale of $(R\mu_f/\gamma)$ to collapse all of their data. Legendre and Maglio [19] investigated the effect of surface wettability on viscous drops with small contact angles. They found that the spreading power law scales as $t^{1/2}$ and then followed by the famous Tanner's law $t^{1/10}$ once the drop attains a spherical cap shape. Biance et al. [20] studied the effect of wettability on the initial stages of spreading for water drops ($V = 5$ μL). The experimental data was found to obey a scaling law with a wetting exponent $n = 0.52 \pm 0.05$. Once the liquid is moving, the factor which limits the dynamics of the spreading is not inertia anymore, but viscosity. The inertial stage is due to the nature of the driving force, which is induced by the gradient of curvature of the liquid–vapour interface.

Furthermore, the effect of relative humidity (RH) on the spreading of colloidal drops has been investigated. Chhasatia et al. [21] demonstrated that the particle deposition area and initial contact angle of aqueous colloidal drops significantly change with RH. A theoretical analysis was presented that is only valid until the contact line first pins and the subsequent decrease of the contact angle with time (constant area mode). The increase in RH results in smaller contact angles, and, therefore, to a larger deposition area for the pinned drop.

Spreading of Newtonian liquids have been largely described in the literature from the hydrodynamic theory [8,10,22]. Few studies have attempted to investigate the spreading of sessile drops of biological fluids. Most studies focus on the spreading and properties, such as shear-thinning and normal stress behaviour, of simple non-Newtonian fluids. Rafai and Bonn [23] investigated the spreading of two model solutions (flexible and stiff polymers) as a function of polymer concentration. Shear-thinning solutions (stiff polymers) followed a power law with a spreading exponent of less than 1/10, whereas normal stress solutions (flexible polymers) exhibited a power law behaviour similar to Tanner's law ($n = 1/10$). The experiments of Rafai et al. [24] found a spreading exponent that is much larger than the 1/10th power of Tanner's law. They attributed their results to Marangoni stresses due to gradients in surfactant concentration. See Table 1 for literature on the spreading dynamics of complex fluids.

The aim of this work was to analyze the effect of the RH on the spreading dynamics of drops of blood. The time evolution of the base radius and the time required for complete spreading of the drop, t_s, were analyzed. Relative humidity was varied from 8% to 90%, and the two spreading dynamics that were observed are discussed.

2. Experimental setup

The initial spreading dynamics of a sessile drop of blood was studied under controlled atmospheric conditions using the set-up shown in Fig. 1(A). The spreading process was performed in a glove box (ambient room temperature, $T_a = 25.5 \pm 0.5\,^\circ$C and a pressure, $P_a = 1005.2 \pm 0.6$ hPa). The volume of this glove box was sufficient to prevent saturation of the atmosphere with the vapour generated. The ambient temperature of the exterior environment was $26.6 \pm 0.3\,^\circ$C. The relative humidity was controlled and measured during each experiment. A range of RH from 8% to 90% was investigated. The experimental conditions for each RH were measured using a weather station. We used ultra-clean microscope glass slide provided by "Thermo Scientific" that were smooth, flat and hydrophilic to blood drops.

Blood samples were collected by a nurse and stored in their 10 ml tubes containing powdered anticoagulant (no surface active agents are added to the whole blood). After, they were placed on a rotating tube to gently mix the whole blood. Typical physical properties of blood such as viscosity $\mu = 10.0$ mPa s and surface tension $\gamma = 69.8$ mN m^{-1} $\pm$ 4.6% has been previously determined in Brutin

Table 1
Literature concerning the spreading dynamics of complex fluids (Exp. for experimental, Num. for numerical and Th. for theoretical).

References	Study	Fluid	Substrate	Spreading regime
[24]	Exp.	Trisiloxane	PET	Power law $n = 1/6$
[23]	Exp.	Polymers	Mica	Similar to Tanner's law
[16]	Exp.	Water	Silicon wafers	Dependent on wettability
[21]	Exp. and Th.	Water suspension	Glass	Dependent on relative humidity
[15]	Num.	Water suspension	–	Independent on wettability
[18]	Exp. and Num.	Water and glycerin	Silicon wafers	Dependent on viscosity
[19]	Num.	Water suspension	Mica	Power law $n = 1/2$
[17]	Exp.	Water and glycerin	Glass	Initial stage independent on wettability
[25]	Exp.	Water and glycerin	Glass	$n = 0.08$ for the 2nd regime

Table 2
Haematology analysis of the blood used in this study. MCV: mean corpuscular volume = haematocrit/red blood cells, MCH: mean corpuscular hemoglobin = (hemoglobin/red blood cells) × 10.

Blood count

Bio-colloids	Typical quantity (units/mm^3)	Typical size (μm)	Volume of colloids (%)
Red blood cells	5.66×10^6	8	97
White blood cells	7.01×10^3	15	2
Platelets	2.05×10^5	3	1

Constants

Hemoglobin (g/dl)	Hematocrit (%)	MCV (fL)	MCH (pg)
16.3	48	85	28.8

et al. [26]. The rheological behaviour of the whole blood has been characterised and determined with a cone/plate rheometer (Anton Paar Physica MCR 501) at a range of shear stress (τ) from 1 to 100 s^{-1} [26]. A non-Newtonian relation between the shear stress τ and the shear rate $\dot{\gamma}$ was found, $\tau = k\dot{\gamma}^n$ (Ostwald–de Waele law), where the power law n was found to be equal to 0.822 ± 0.01, and k is the consistency. Therefore, the whole blood behaves as a shear-thinning fluid [27] since the viscosity decreases with the shear rate. The relationship between blood viscosity (μ) and shear rate ($\dot{\gamma}$) depends on red blood cells concentration [28]. Indeed, the increase of biocolloids concentration, increases the viscosity and thus, the non-Newtonian behaviour of the fluid. However, the blood viscosity ($\mu = \tau/\dot{\gamma}$) is approximately ten times higher than that of water. In our study, the whole blood viscosity μ is equal to 10.0 mPa s and increases by 29% when the temperature of whole blood decreases from 37 °C (human body temperature) to the ambient temperature $T_a = 25$ °C [29]. A full hematological and biochemical analysis of the blood was also performed to obtain the biological characteristics of blood. Blood is a complex fluid composed of a liquid phase (plasma) and cellular matter (red blood cells, white blood cells, and platelets). These biocolloids are described in Table 2 in terms of quantities, sizes, volumes and other constants. The red blood cells accounts for 97% of the colloids volume and 85 fL (Femtoliter) of mean corpuscular volume based on a hematology analysis. All experiments were performed within a period of 8 h.

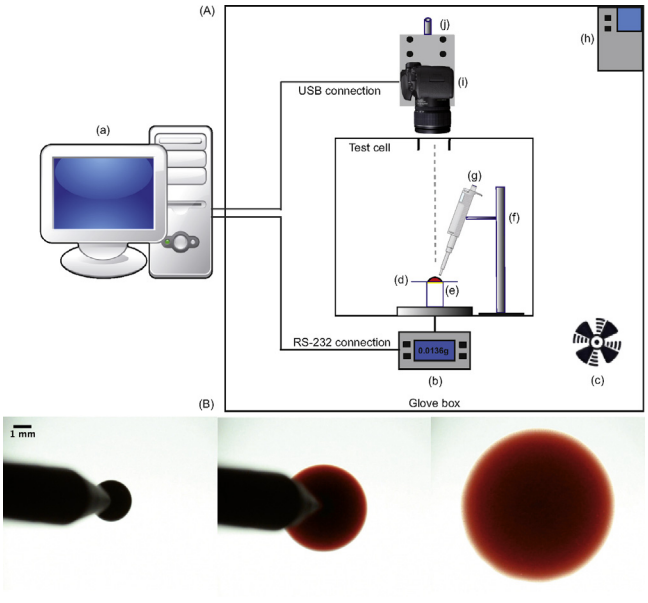

Fig. 1. (A) Equipment used to study drop spreading dynamics: a computer (a), digital balance (b), fan to recirculate air inside the box (prior to the experiment) (c), glass substrate (d), cold back-light source (e), levelling system to control the micropipette position (f), digital micropipette (g), humidity controller (h), levelling high-precision screw to control the camera position (j) and EOS 7 HD digital camera operating at 50 frames per second. (B) Series of top view images (from left to right) captured during the last frame before contact ($t = 0.2$ s), immediately after the drop touched the glass substrate and after the drop of blood completely spread on the ultra-clean glass substrate.

Drops of blood of small volume are performed using a digital micropipette (Eppendorf Stream) to form a drop of precise volume ($V = 14.2\ \mu l \pm 1.0\%$) on the clean glass substrate. The needle was fixed at a short distance from the glass slide (but not contacting) to minimize the kinetic energy of the falling drop.

Before contact, a dark circular area at the tip of the needle was observed (Fig. 1(B), left image). When the spherical drop touched the substrate (Fig. 1(B), center image), the drop of blood began to wet the glass substrate with an initial deposit radius, R_0 and spread until it achieved a maximum radius. The spreading stops when the triple line gets pinned forming a final deposit radius, R_f (Fig. 1(B), right image) and a contact angle θ with the glass substrate. Simultaneously, we used a digital camera (Canon EOS 7D) coupled with a 1–5× macro-lens to record the top-view of the wetted area. The digital camera (resolution of 1280×720 pixels on an area of 22.3×14.9 mm^3) operates at a typical frame rate of 50 frames per second, which is acceptable to monitor the spreading process of a drop of blood. Then, the video was recorded onto a computer disk, and each image was analyzed using an image processing system.

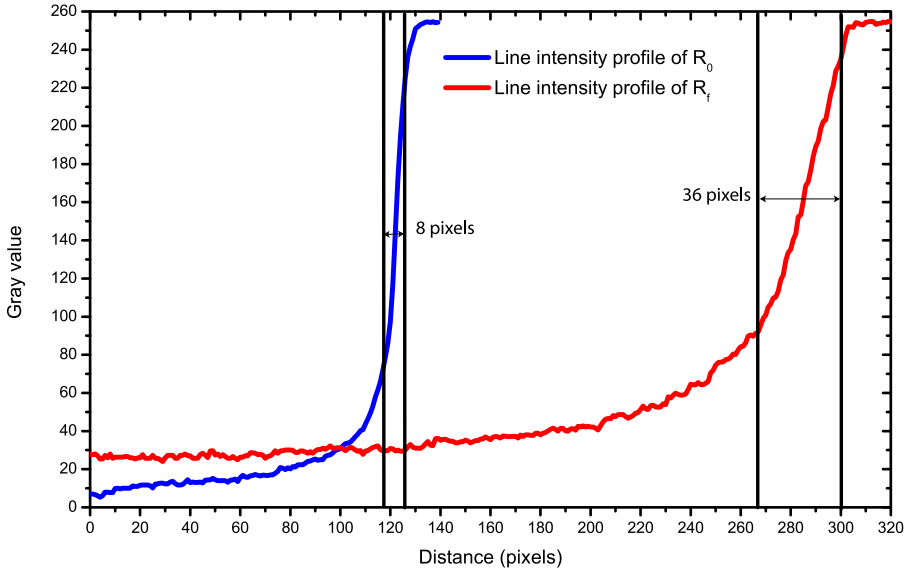

Fig. 2. Intensity along the straight line of an initial deposited radius R_0 and of a final wetted radius R_f. The bars given in the plot show that the measured uncertainty of R_f is higher than that of R_0.

The drop was back-lit by a cold cathode light at 5000 K ± 270 K to homogenise the luminous intensity and improve the contrast. The effect of the density of light was studied to avoid any biological or chemical disturbance on the phenomenon.

Initial mass, m_0, was recorded using a digital high-precision balance (Mettler Toledo XS 105) with a resolution of 10 μg at 10 Hz. Contact angle (angle between the spherical cap and the solid surface) is calculated using Eq. (1) in Section 3. This contact angle is an apparent contact angle θ_{app} as opposed to the classical microscopic one which is far below the scale of observation. The recorded images were processed using IMAGEJ®. The contact line of the bottom images is detected using a circular fit of multi-points in order to overcome any axisymmetric problem that could occurs during the spreading process. Because of contrast variation at the edge of the blood drop, the error bars given in the plots correspond to an uncertainty of 4 pixels in the initial deposited radius (65 microns), R_0, and 18 pixels in the maximum wetted radius (291 microns), R_f, as shown in Fig. 2. The error in the apparent contact angle, $\delta\theta_{app}$, was calculated using the uncertainty of the maximum and minimum contact radius. The mean velocity of the triple line, $\overline{U}$, was calculated using the following equation: $\overline{U} = (R_f - R_0)/t_s$, where t_s is the total spreading time. Contact (t = 0 s) occurs between the last five frames where the drop becomes detached from the needle and the first frame where the wetted area appears. Given the frame rate, the uncertainty in the start time is 0.1 s for each experiment.

3. Full description of spreading dynamics

In this section we describe the dynamics of a blood drop as it contacts and subsequently wets a clean glass substrate at a specified RH. Fig. 3 shows the radius, R, of the wetted area as a function of time for a drop of blood with an initial deposited radius of R_0 = 2.17 mm at 65% RH. As the drop of blood spread on the glass substrate, the triple line moved radially outwards with a mean velocity of $\overline{U}$. Drops

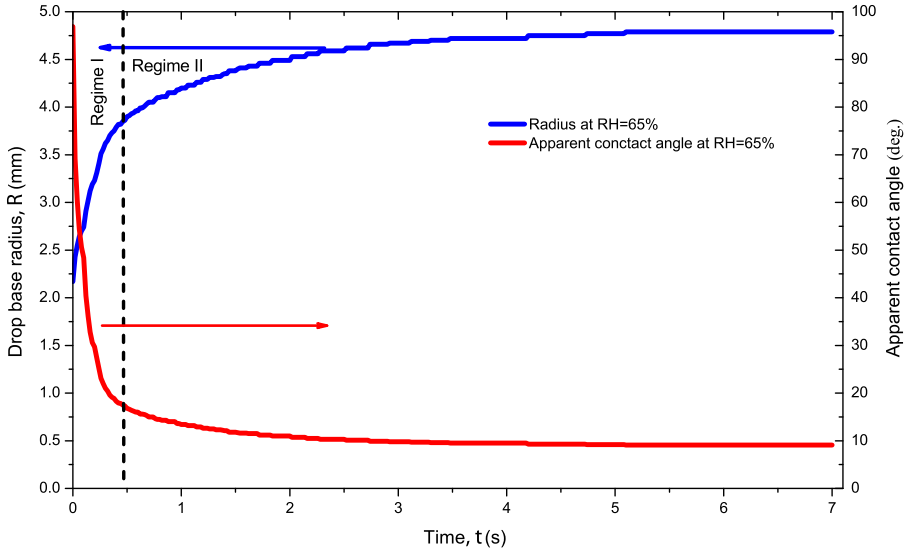

Fig. 3. Evolution of the radius of the wetted area, R, and the apparent contact angle, θ_{app}, as a function of time, t, for a drop of blood with an initial deposited radius of R_0 = 2.17 mm (RH = (65.0 ± 2.0)%, T_a = (25.5 ± 0.5) °C, P_a = (1005.2 ± 0.6) hPa). Regime 1: Spreading regime corresponds to competition between viscous forces and capillary forces. Regime 2: Spreading corresponds to competition between viscous dissipation and rate of evaporation.

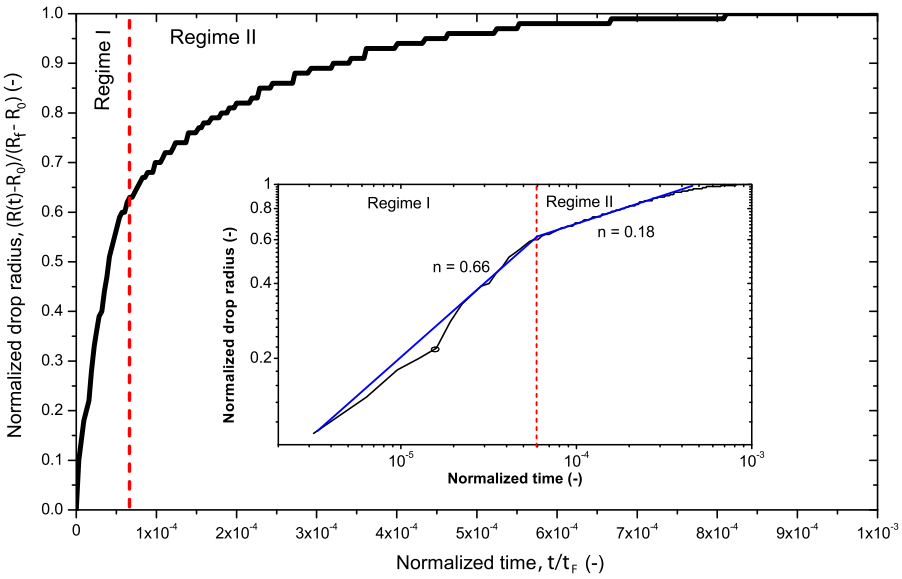

Fig. 4. Evolution of the dimensionless radius, $(r(t) - R_0)/(R_f - R_0)$, as a function of dimensionless time, t/t_F, at RH = 65%. The inset graph is a plot in a log-log representation.

of blood spread from the initial deposit radius R_0 and wet a circular area of final contact line radius R_f.

Later, after complete spreading at the total time of spreading, t_s, the contact line stopped moving and was pinned as shown by the plateau in Fig. 3. The dashed line was placed where a sharp change (cross-over) to a slower dynamics is observed. The total time of spreading corresponds to the time required for the contact line to become pinned. Indeed, in the case of biological fluids, proteins adsorb to the substrate, which anchors the triple line [30]. However, an evaporative outward flow motion (Marangoni flow) induced by solvent evaporation displaces micrometre-sized particles (biocolloids) towards the pinned contact line [26]. These particles further enhance contact line pinning. Therefore, for a small drop (= 14.2 μl ± 1%) with a contact base radius that is less than or equal to the capillary length $l_c = \sqrt{\gamma/\rho g}$, the fluid spreads as a spherical cap shape with a circular base area at every moment in time because gravitational forces are negligible. This implies that the instantaneous configuration of the drop can be fully described by the time-dependent base radius, $r(t)$, where $r(t)$ is the wetting radius of the spreading droplet.

Moreover, Fig. 3 also shows the decrease in contact angle as a function of the spreading time at 65% RH. However, the contact angle decreases to 9.1 deg. during the final stages of spreading. The low roughness and surface energy of the glass substrate caused the blood to behave hydrophilically on the clean glass substrate, and a contact angle of less than 40° was observed. This contact angle can be expressed as a function of the final radius of the wetted area, R_f, and the initial experimental volume of the drop, V_{exp} [31]:

$$\theta_{app} = \frac{4V_{\exp}}{\pi R_f^3}, \quad (1)$$

However, we clearly distinguished two regimes in the spreading behaviour. During the first regime of spreading (i.e., the initial stages of spreading), the dynamics are fast with an average contact line speed of approximately 1.92 mm s^{-1}. The second regime of spreading is much slower than the first, with an average contact line speed of approximately 0.11 mm s^{-1}. The crossover in between these two regimes occurred at time t = 0.40 s after contact for a contact line radius of R = 3.79 mm and an apparent contact angle of θ_{app} = 17.9°. The spreading stopped when the drop reached its equilibrium shape (R_f = 3.79 mm and θ_{app} = 9.1°). We were able to better characterise spreading dynamics by nondimensionalising the data in Fig. 3 (drop base radius). Zero time is defined by subtracting the contact line radius, $r(t)$, from the initial deposited radius, R_0, and scaling it with the final contact radius of the drop, R_f [$R^* = (r(t) - R_0)/(R_f - R_0)$]. Therefore, this scaling enabled us to precisely determine the drop profile because the drop started to spread with an initial deposited radius, R_0. There are two possible timescales to consider. If the capillary forces driving the flow are primarily hindered by viscosity, then the characteristic timescale is t_D. Eddi et al. [17] obtained the following equation to describe the dynamics of viscous drop spreading:

$$r^* = -a\frac{t}{t_D}\ln\frac{r}{R}, \quad \text{with} \quad t_D = \frac{4\pi\mu R_f}{\gamma}, \quad (2)$$

where a is used as an adjustable parameter, μ is the viscosity, $r^* = r/R$ is the normalized radius and γ is the interfacial tension between the drop of blood and surrounding air. However, if the spreading is influenced by the difference between the saturated pressure and the air pressure, then the characteristic timescale is t_F. For our experimental situation, a low-volatility fluid spread under natural conditions, and the evaporation process was limited by the diffusion of water into air. Thus, a diffusion model was used to predict the total evaporation time, t_F [32]:

$$t_F = \frac{4RTm_0}{\pi\Delta P D_f D_{diff}}, \quad (3)$$

where D_{diff} the coefficient of diffusion, T is the air temperature, R is the gas constant, m_0 is the initial drop mass, D_f is the final wetting diameter of the wetted area, and ΔP is the difference between the saturated pressure and the air pressure. Fig. 4 shows how the results in Fig. 3 were rescaled using the timescale, t_F. A log-log plot of the same data reveals that the position of the contact radius follows a power-law growth. We determined the power exponents for the first and second regime of spreading by a linear fit of the data. We did not rescale the data shown in Fig. 3 with t_D because the curve shows similar spreading to that in Fig. 4.

4. Influence of relative humidity on spreading dynamics

To quantify the effects of the RH on the spreading dynamics, we measured the spreading radius, $r(t)$, of drops of blood of twelve different humidities. Details of the experimental setup for each RH are summarised in Table 3. The results are shown in Fig. 5 and

Table 3
Experimental details regarding the spreading of a blood drop of volume $V = 14.2\,\mu l \pm 1.0\%$ on a microscope glass substrate with different humidities ($\Delta m_0 = \pm 0.10$ mg, $\Delta t_s = \pm 0.57$ s, $\Delta D_f = \pm 0.18$ mm).

RH (%)	ΔRH (%)	m_0 (mg)	D_f (mm)	θ_{app} (deg.)	$\Delta\theta_{app}$ (%)	U (mm s^{-1})	ΔU (%)	t_s (s)	t_F (min)	Δt_F (%)	t_D (ms)	Δt_D (%)
8	2	14.1	7.76	16.9	6.1	1.32	7.6	1.52	50	4.6	6.99	6.5
13	2	14.8	7.87	17.0	5.8	0.94	7.4	1.64	55	4.6	7.09	6.5
20	2	14.7	8.10	15.5	5.9	1.14	6.8	1.72	58	4.6	7.29	6.5
30	1	12.2	8.21	12.4	5.7	0.93	6.6	1.86	54	4.6	7.39	6.5
35	1	13.6	8.63	11.9	5.5	0.83	5.6	2.24	62	4.5	7.77	6.5
39	1	14.2	8.67	12.2	5.5	0.67	4.8	2.82	68	4.5	7.80	6.5
50	2	12.8	8.55	11.5	5.5	0.46	5.0	3.16	76	4.5	7.70	6.5
54	2	10.2	8.02	11.1	5.7	0.43	5.2	3.18	70	4.6	7.22	6.5
65	2	14.2	9.57	9.1	4.9	0.51	3.0	5.10	108	4.4	8.62	6.4
75	2	13.8	9.80	8.2	4.8	0.44	2.4	6.78	143	4.4	8.82	6.4
82	2	14.2	10.44	7.0	4.5	0.38	2.0	9.10	192	4.4	9.40	6.3
90	2	13.4	11.35	5.1	4.1	0.25	1.7	14.32	300	4.3	10.20	6.3

illustrate that drops spread faster at high evaporative rates (low RH) than low evaporative rates (high RH). Consequently, the total time of spreading, t_s, increases with RH. Furthermore, all curves exhibit the same qualitative behaviour, as characterised by the two distinct spreading regimes shown in the previous section.

When a drop of blood contacts the hydrophilic surface, the drop spreads over the solid to minimize the total surface energy. For small drops, whose radii are smaller than the capillary length, the effects of gravity are negligible and spreading is driven by capillary forces. The capillary number ($Ca = \overline{U}\mu/\gamma \approx 1.1 \times 10^{-6}$), where $\overline{U}$ is the average speed estimated using a RBC displacement ($\overline{U} \approx 8\,\mu m\,s^{-1}$), compares the viscous and capillary forces and was determined for a drop of blood in a previous study [26]. It is assumed to be extremely small. Consequently, capillary forces dominate the flow motion inside drops of blood. In the first regime of spreading, the surface of the drop significantly deforms as a capillary flow travels along the surface of the drop. In this regime, capillary forces rapidly drive spreading because of the curved surface, whereas the viscous forces of the fluid resist deformation. Once the capillary flow has dissipated, the spreading liquid enters a second regime. In this regime, the drop continues to spread, but at a significantly slower rate. Then, the spreading of the drop of blood takes the form of a spherical cap with a decreased contact angle, and the surface energy gained by spreading is balanced by the viscous dissipation associated with this motion [6]. However, the drop of blood starts to spread in a surrounding air composed of vapour concentration that increases with RH. Therefore, a high RH reduces the net flow of evaporating water molecules, which decreases the effective surface tension on the drop surface and thus the balanced forces. Consequently, the spreading dynamics decreases and the spreading time t_s increases.

Furthermore, as RH decreased, the global rate of evaporation increases and thus the internal flow motion inside the drop. This increase in the internal flow velocity enhanced the transportation mechanism of biocolloids towards the edge of the blood drop. Thus, red blood cells are quickly adhered to the substrate to enhance the pining of the triple line inducing a rapid spreading time. More explanation will be provided in the next section. This mechanism is found identical to that of pinned drying drops of nanofluids where increased RH, increases the time of pattern formation [33]. Because drops of blood are composed of high concentration of 8 μm-sized particles, concentration and determined haematological constant presented in Table 2, play an important role in driving the flow motion and on blood viscosity. A high concentration of red blood cells would slightly increase the blood viscosity and hence affects the spreading dynamics (decreased triple line velocity).

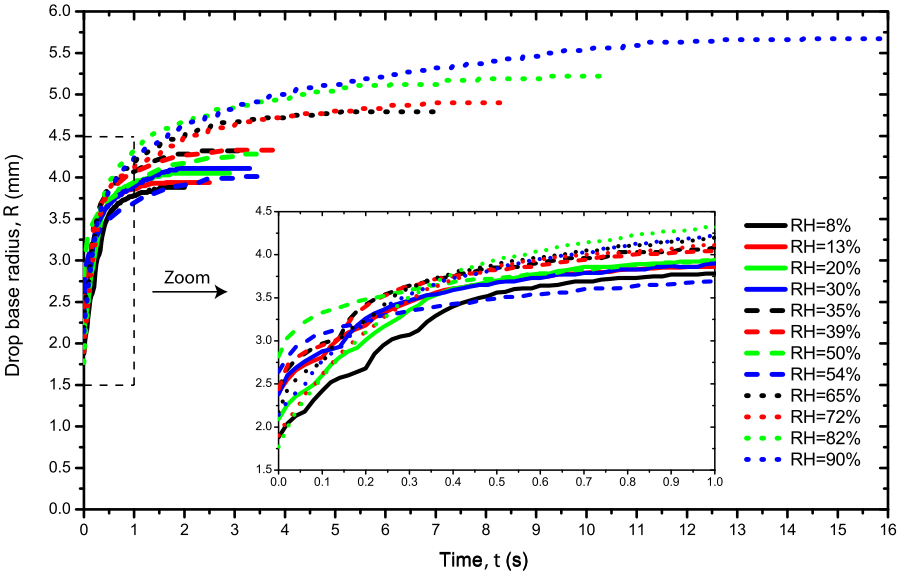

Fig. 5. (a) Evolution of the radius R as a function of time t for drops of blood with viscosity $\mu = 10.0$ mPa s and initial deposited radius (average deposit radius: $\overline{R}_0 = 2.3 \pm 0.3$ mm) for different humidities ranging from 8% to 90%. All experiments were performed on the same drop volume $V = 14.2\,\mu l \pm 1.0\%$ ($m = 13.5$ mg $\pm 9.5\%$, $T_a = (25.5 \pm 0.5)$ °C, $P_a = (1005.2 \pm 0.5)$ hPa). The inset graph is a magnification of the spreading time from 0 to 1 s.

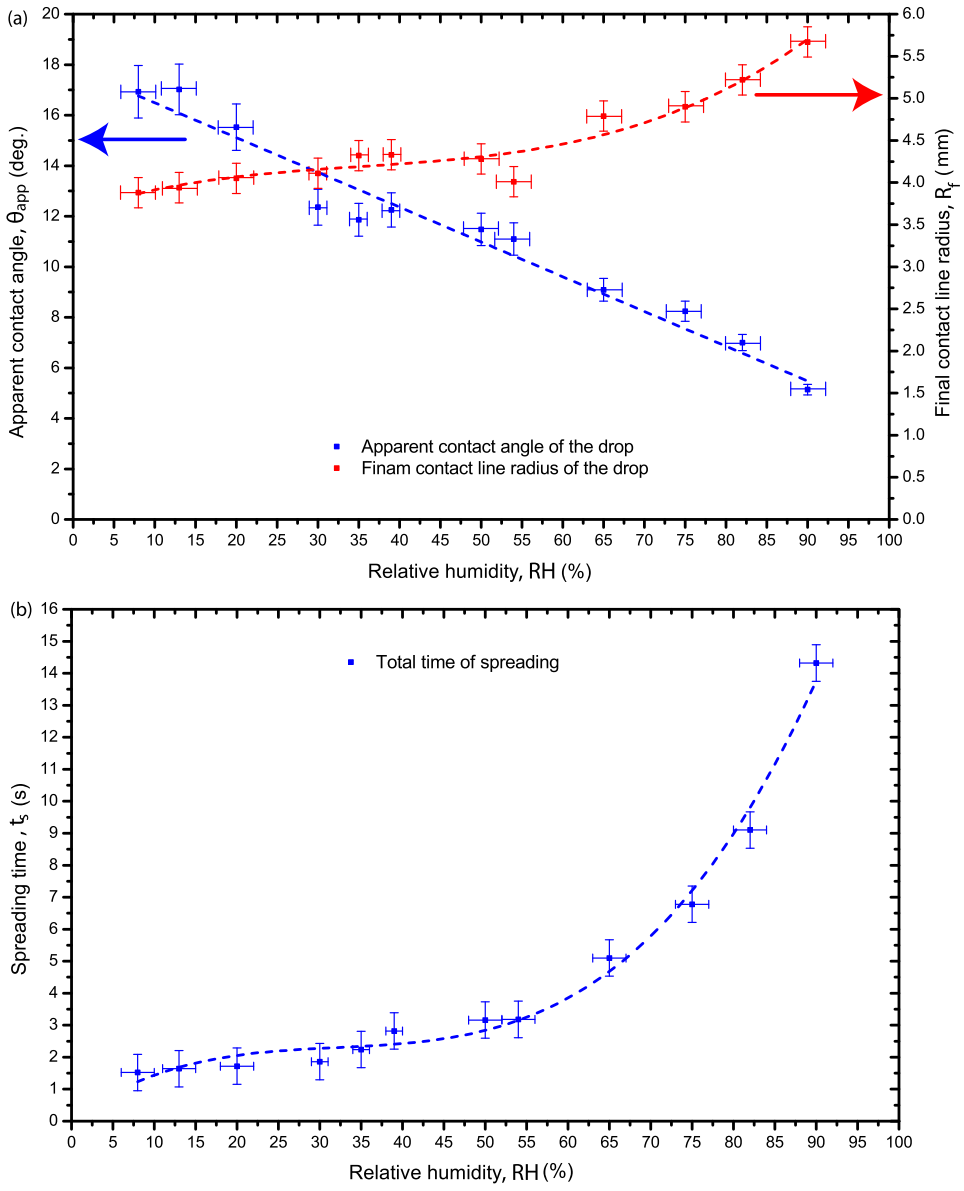

Fig. 6. (a) Variation of the apparent contact angle θ_{app} of the drop of blood as a function of the RH ($T_a = (25.5 \pm 0.5)$ °C, $P_a = (1005.2 \pm 0.6)$ hPa). The blue dashed line is the linear fit for the apparent contact angle [$\theta_{app} = axRH + b$ with $a = -0.24 \pm 5.9$ % and $b = 0.31 \pm 2.2$ %], passing by the measurement points. The red dashed line is the cubic fit of the final contact line radius [$R_f = a + bxRH + cxRH^2 + dxRH^3$ with $a = 3.6 \times 10^{-3}$, $b = 3.3 \times 10^{-3}$, $c = -7.5 \times 10^{-3}$, $d = 7.1 \times 10^{-3}$ and $R^2 = 0.92$], passing by the measurement points. (b) Variation of the total spreading time t_s of the drop of blood as a function of the RH. The blue dashed line is the cubic fit of the total spreading time [$t_s = a + bxRH + cxRH^2 + dxRH^3$ with $a = 8.2 \times 10^{-2}$, $b = 1.8 \times 10^{-1}$, $c = 5.3 \times 10^{-3}$, $d = 5.5 \times 10^{-5}$ and $R^2 = 0.97$], passing by the measurement points. (For interpretation of the references to colour in this figure legend, the reader is referred to the web version of the article.)

Fig. 6 shows the total time of spreading as a function of various RH. At 8% RH, the total time of spreading is 1.52 s, which increased with RH. Moreover, Fig. 6 shows a linear decrease in the apparent contact angle with RH. This linear decrease in the apparent contact angle causes an increase in the final contact line radius, R_f [34,35].

When the pendant drop is brought into contact with the glass substrate, the drop of blood spreads to its maximum radius with a contact line velocity proportional to the rate of evaporation (Table 3). However, at lower evaporative rates (high RH), the triple line velocity decreased and, consequently, increased the total time of spreading for drops of blood. A higher apparent contact angle was observed at higher evaporative rates, which can be attributed to a short total spreading time. An explanation is based on the contact line velocity and the time required for the triple line to become pinned during the spreading process. This process is affected by the evaporation rate at the initial stages of spreading, as previously discussed. A contact line with high concentration of biocolloids spreading at different RH modifies the interfacial tensions between the solid, liquid and vapour acting at the three phase triple line. Consequently, the new equilibrium contact angle is affected by both the concentration of biocolloids and the rate of evaporation [34,35]. The biocolloids help to pin the triple line; a high evaporation rate decreases the total time of spreading. Chhasatia et al. [21] experimentally showed an increase in spreading dynamics and a decrease in the initial contact angle with increased RH. He also showed an increased in the theoretical time for pico-litre droplets with increasing RH (0.8 s at 10% and 1.5 s at 60%). In their experiments, the authors introduced a function that relates the dynamic contact angle to the rate of evaporation using previous empirical studies on the spreading of nonvolatile liquids.

To investigate the effect of the theoretical evaporative time, t_F, on the drop spreading dynamics, the experimental spreading

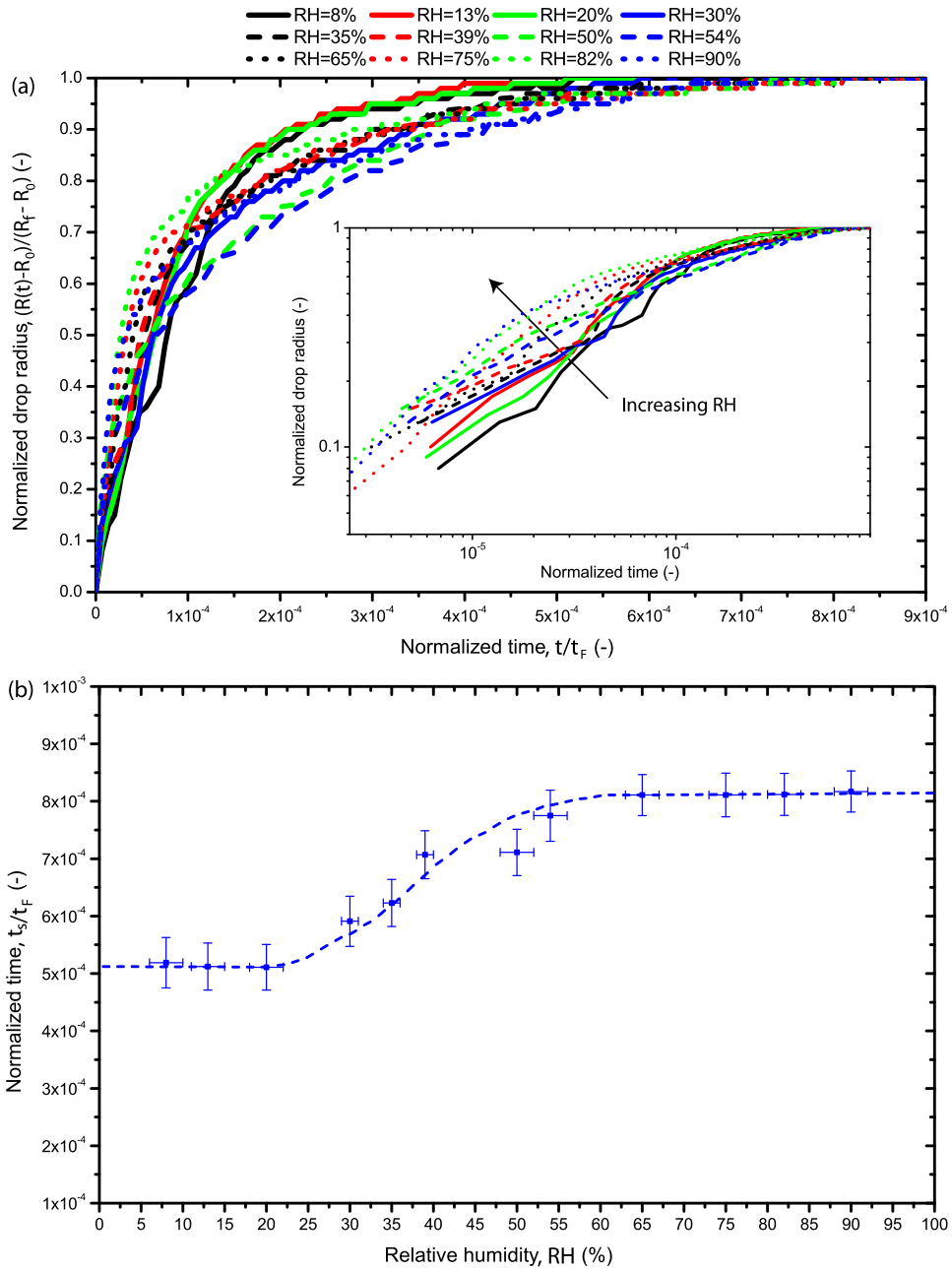

Fig. 7. (a) Normalized drop radius, $(r(t) - R_0)/(R_f - R_0)$, as a function of normalized time, t/t_F, for different humidities, and (b) Normalized total time of spreading, t_s/t_F, as a function of RH. The inset graph is a log-log representation for all RH values.

time for each RH was scaled by the theoretical evaporative time, t_F, for that RH value (Fig. 7(a)). All the curves exhibit the same dynamic behaviour in the first regime of spreading. Subsequently, reduced spreading was observed in the second regime, and spreading stopped when the contact line reached its maximum radius and was pinned. However, to gain more insight into the late spreading process (i.e., the second regime of spreading), the total time of spreading t_s was scaled by the theoretical evaporative time, t_F, and plotted as a function of RH (Fig. 7(b)). We observed a collapse of the data in the late spreading process ($t_s/t_F = 6.83 \times 10^{-4} \pm 18.5\%$). This result implies that the dynamics of drop spreading depend on the theoretical evaporative time, t_F, (given by the dimensionless time t_s/t_F) at later stages of the spreading process.

Furthermore, the effect of the theoretical time, t_D, on the dynamics of drop spreading was investigated by scaling the experimental time of spreading for each RH by the theoretical time, t_D, for that RH value (Fig. 8(a)). At early times of spreading (for t/t_D less than 100), all experimental radius curves collapse on each other (inset graph of Fig. 8(a)). However, as RH increased, drop spreading appeared to depend on the theoretical time, t_D. At late times of spreading, each of the experimental curves undergoes a transition and presents a sharp change to slower dynamics with increased RH. To gain more insight into the second regime of spreading, the total time of spreading, t_s, was scaled by the theoretical time, t_D, and plotted as a function of RH (Fig. 8(b)).

However, normalized time t_s/t_D increases with RH and follows a polynomial fit (Fig. 8(b)). This result indicates that at early times the dynamics of drop spreading depend on the theoretical time, t_D, (given by the normalized time t_s/t_D), whereas at late times of spreading, t_D plays an important role at different RH. For the first

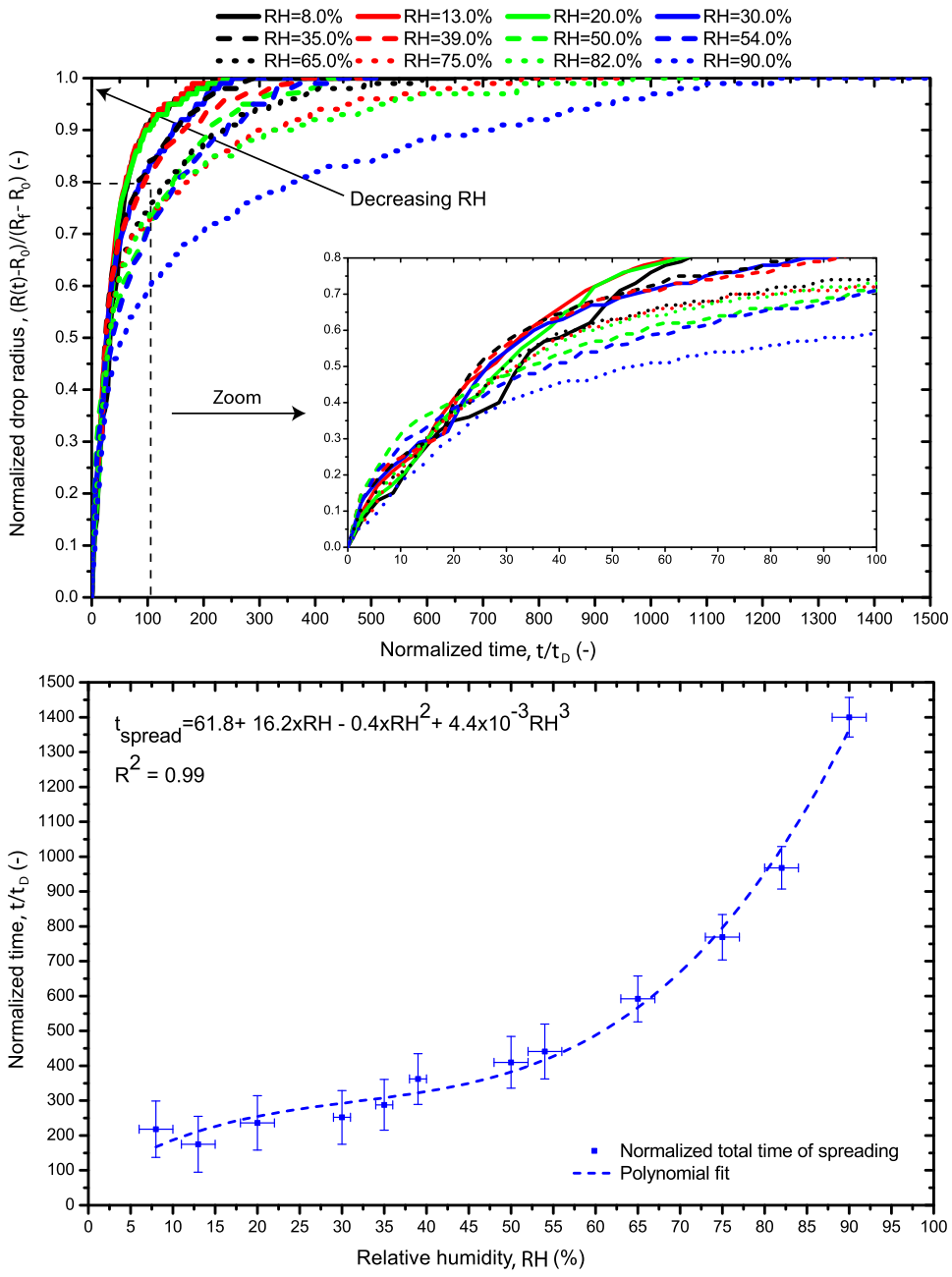

Fig. 8. (a) Normalized drop radius, $(r(t)-R_0)/(R_f-R_0)$, as a function of normalized time, t/t_D, for RH varying from 8% to 90%. The inset graph is a magnification of t/t_D from 0 to 100. (b) Normalized total time of spreading, t_s/t_D, as a function of RH.

regime of spreading, the radius can be expressed by a power law of the form $(r(t)-R_0)/(R_f-R_0)=k\times(t/t_D)^n$, with $k=2.19\times10^{-2}$ and $n=0.65\pm0.11$. This power law was obtained by fitting all the experimental curves.

We have shown that early spreading of blood drop on an ultra clean glass substrate is controlled by the competition between viscous and surface tension forces as defined by the theoretical time, t_D. During the initial stages of spreading, the evolution of the wetted area growth as $\sim(t/t_D)^{0.65}$. The prefactor remained the same as the RH increased. The data curves separated at approximately $t/t_D\sim100$ after contact, showing a dependence on the rate of evaporation. Furthermore, at late stages of spreading, we scaled our data by the theoretical evaporative time, t_F, which considers the difference between the saturated pressure and the air pressure, and found that our data collapsed for varying RHs. The radius can be expressed by a power law of the form $(r(t)-R_0)/(R_f-R_0)\sim(t/t_F)^n$ with $n=0.19\pm0.03$. This power law was obtained by fitting all the experimental curves. At this stage, a continuous liquid phase was not in contact with the solid. Because blood is a complex fluid composed of micrometre-sized particles, the particle nature of the fluid has a significant effect on the flow motion. These particles further enhance contact line pinning and are transported by flow motion that depends on the evaporative rate. Eddi et al. [17] performed experiments with droplets of a homogeneous mixture (water–glycerin) on four different substrates of variable wettability (from $\theta=0^\circ$ to $\theta=105^\circ$). They observed the scaling law $r(t)\sim t^{1/2}$ at the initial stages of spreading (inertia dominated regime) whereas Legendre and Maglio ([19]) obtained a spreading exponent of 2/3 when the balance is controlled by viscous-capillary forces. Vapour molecules become more saturated with increasing RH,

Table 4
Estimation of characteristic dimensionless numbers for the two regimes of blood drop spreading at RH = 65%.

Number	Formula	Signification	Regime I	Regime II	Ratio I/II
$\overline{R}$ (mm)	–	Mean radius	3.18	4.54	0.7
$\overline{h}$ (mm)	$\overline{R}((1-\cos(\theta))/\sin(\theta))$	Mean height	1.05	0.41	2.5
$\overline{U}$ (mm s^{-1})	–	Mean velocity	1.92	0.11	17.4
Re	$\rho\overline{U}\overline{h}/\mu$	Inertia/viscous	0.209	0.004	44.4
Ca	$\mu\overline{U}/\gamma$	Viscous/capillary	2.75×10^{-4}	1.58×10^{-5}	17.0
Bo	$\rho g\overline{h}^2/\gamma$	Gravity/capillary	0.160	0.024	6.5
We	$\rho\overline{U}^2\overline{h}/\gamma$	Inertia/capillary	5.74×10^{-5}	7.41×10^{-8}	774
Fr	$\overline{U}^2/g\overline{h}$	Inertia/gravity	3.59×10^{-4}	3.00×10^{-6}	120
St	$\mu\overline{U}/\rho g\overline{h}^2$	Viscous/gravity	1.72×10^{-3}	6.38×10^{-4}	2.7

which reduces the effective surface tension of the drop. However, total spreading time increases and important dependence with the RH shows up.

5. Discussion

We have shown that the first spreading regime depends on the characteristic time t_D (competition between viscous forces and capillary forces), and the second spreading regime depends on the characteristic time t_F (competition between viscous dissipation and the rate of evaporation). Increased RH reduces the spreading dynamics over total spreading time, t_s. Four different forces are involved in drop spreading: gravity, capillary, viscous and inertia forces. These four forces were compared to determine the dominating contribution during drop spreading. An estimation of relevant dimensionless numbers that was used to quantitatively characterise the dominant mechanisms involved in the drop spreading process is provided in Table 4. The Reynolds number (*Re*) for internal blood drop flow compares inertial forces to viscous forces, the Capillary number (*Ca*) compares viscous forces to capillary forces, the Bond number (*Bo*) determines the relative importance of the gravity compared to capillarity effects, the Froud number (*Fr*) compares inertial forces to gravitational forces, the Weber number (*We*) compares inertial forces to capillary forces and Stokes number (*St*) compares viscous forces to gravitational forces. Additionally, $\overline{U}$ is the mean spreading velocity of the triple line, which is assumed to be close to the fluid flow in the droplet at the triple line, ρ is the whole blood density, R is the drop radius, h is the drop height and g is the gravitational acceleration. Typical values for these three variables are presented in Table 4. From values for dimensionless numbers presented in Table 4, it was concluded that $F_{capillary} > F_{gravity} > F_{viscosity} > F_{inertia}$. The magnitude of *Bo* and *Re* indicates the effects of gravity and inertia on the drop spreading, respectively. These dimensionless numbers are smaller in the second low-speed spreading regime than in the first high-speed spreading regime. Because our drops have small volume and all these dimensionless numbers are all small during the entire spreading process, it was concluded that the spreading is dominated by capillary forces, especially in the second low-speed spreading regime. This second regime is also governed by viscous forces. In both regimes, the calculation of the Bond number ($Bo > 1$), revealed that the shape of the drops can be considered to be a hemispherical cap and that gravitational effects can be neglected because it adds only a small contribution to the flow compared to capillary forces.

Upon contact with the microscope glass substrate, the drop of blood starts to evaporate with an evaporative mass flux J that is proportional to the vapour concentration between the drop surface and the air. In our experiments, water evaporation was assumed to be at a quasi-steady state because $C_v(1-H)/\rho$ is negligible (where C_v is the water vapour concentration); thus the diffusion time was far shorter than the characteristic time of evaporation. In the diffusive-limited case, the evaporative mass flux, *J*, along the blood drop surface is not uniform and tends to diverge in the vicinity of the triple line [36]. The singular corner geometry of the droplet close to the contact line supports a diverging evaporative flux and, therefore, a diverging velocity field [37–39]. Upon spreading of the blood drop, the triple line velocity scaled with internal flow motion due to evaporative mass flux. This internal flow motion transports the colloids and liquid towards the rim to replenish the liquid at the edge of the triple line that evaporates significantly faster [36]. However, this internal flow is driven only by Marangoni convection [26]. For small contact angles, as the contact line is approached, the evaporative flux diverges with velocity field $u(\rho,\theta) = (1/\rho_l)](\rho)$, where ρ_l is the liquid density [39].

Hydrodynamic theory emphasises dissipation due to viscous flow within the wedge of liquid near the moving contact line [8,5]. Thus, changes in the apparent macroscopic dynamic contact angle θ_{app} were attributed to viscous bending of the liquid vapour interface within the mesoscopic region. By assuming that the Capillary number is extremely small and that the curvature of the outer liquid is small, [5] derived a relationship for the apparent contact angle ($\theta_{app}^3 \sim \mathrm{Ca} \approx \mu U/\gamma$) based on asymptotic theory. Then, Tanner [6] considered a similar situation for a viscous drop spreading on a completely wetted substrate in which a precursor film is formed prior to the drop. For late times of spreading, the authors proposed a law which is known as Tanner's law:

$$r(t) = 0.84.V^{3/10}(\gamma t/\mu)^{1/10}, \tag{4}$$

After derivation, Eq. (4) leads to the velocity of the contact line *U*:

$$U = \frac{dR}{dt} = \frac{\gamma}{100\mu}\left(\frac{4}{\pi}\right)^3\frac{V^3}{R^9}, \tag{5}$$

However, the intensity of evaporation scales with flow motion. Increased rate of evaporation was observed in the vicinity of the triple line at high evaporative rates (Fig. 9(a)), compared to low evaporative rates (Fig. 9(b)). Therefore, there was an increase in the amount of liquid and colloids that helped to move the triple line forward, which enhanced the internal flow and replenished the loss of water caused by the high evaporation rate. Consequently, the mean velocity in the vicinity of the triple line decreased with RH as shown in Fig. 10. In this figure, our experimental results are smaller than those attained using Tanner's model but increase at high RH. Experimental volume and final wetted radius are introduced in Eq. (5) in order to calculate theoretical velocity. An explanation is that calculating the mean velocity considers both regimes, whereas Tanner's model is based only on the second low-speed regime. Furthermore, the local viscosity in the vicinity of the triple line increases during spreading because an increase in the amount of micrometre-sized particles modifies the viscosity and the velocity of the triple line [40].

When the blood drop wets the glass substrate, the evolution of the wetted drop radius depends on the dominant physical forces that are driving and resisting the spreading. At the early stage of

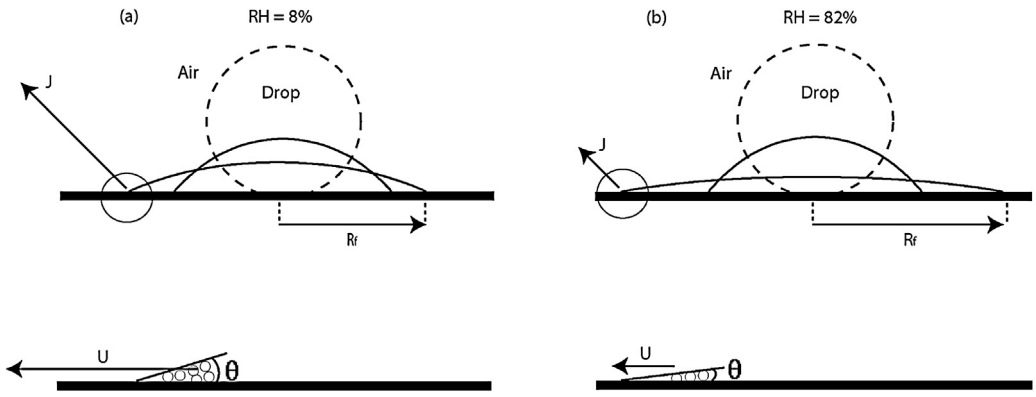

Fig. 9. Schematic representation of spreading drops for the case of: (a) RH = 10% and (b) RH = 80%. Initially, the blood drop has a spherical shape, and at equilibrium the drop has the shape of a spherical cap. The arrows indicate the velocity and evaporative flux of water vapour from the drop surface to the surroundings in the vicinity of the triple line. The dashed square marks the area close to the triple line, where the drop geometry can be approximated by a wedge.

spreading, capillarity acts as the driving force and viscous flow throughout the spherical cap provides the resistance. Scaling by viscous-capillary characteristic time t_D gives a power law evolution $r(t) \sim t^n$ ($n = 0.65$) for different humidities. Such evolution is found to be in agreement with the experiments of Legendre and Maglio [19]. For a viscosity equal or larger than 0.01 Pa s, the authors observed a spreading exponent of 2/3 when the corresponding viscous-capillary characteristic time $t_\mu = \mu R_0/\gamma$ is used.

Fig. 11 presents the power law exponent as a function of RH compared to Tanner's model. The spreading exponent of the second regime of spreading is found to be higher than that of Tanner's law for all different humidities. Drops of blood spread much more slowly in the second regime compared to the first one as expected because of the large viscous forces in the thin film reducing the spreading speed. When the blood drop enters this second regime of spreading, gravitational forces can be balanced with viscous forces and add a small contribution to the flow. Thus, this gravitational forces can lead to an acceleration in the spreading ($R \propto t^{1/8}$) and a small deviation from Tanner's law [41]. This deviation is too small to account for the high observed values of the spreading exponent. Therefore, there must be an additional driving force for the second regime of spreading, leading to the fast dynamics. Blood is a complex colloidal suspension for which the flow motion is non-Newtonian. At the beginning of drop evaporation, the fluid is homogeneous in colloids. When drops of blood evaporate, RBCs are carried out by Marangoni flow and accumulate at the triple line [26]. Furthermore, since the evaporative flux is higher at the triple line, spatial gradients in the RBCs concentration and/or temperature can drive strong secondary flows and thus, the balance between the Marangoni stresses and the viscous dissipation near the liquid wedge. When RH decreases, the evaporative flux at the triple line becomes stronger as discussed before. Marangoni flow induced by both solvent evaporation and concentration gradients could be a driving force to enhance the spreading rate of the second regime. Such evaporatively driven Marangoni flows lead to formation of coffee rings [37]. Rafai et al. [24] found a spreading exponent between 1/4 and 1 due to gradient in surfactant concentration that is established both in the radial and in the height direction. Also, peculiar form of the drop shows that the capillary forces are dominated by the driving force such as in gradients in surfactants concentration [42,43,23]. In our case of partial wetting, the blood drop after deposition spreads out until it reaches in equilibrium contact angle. This latter can be expressed as a function of the disjoining pressure [44,45] that it may be present when a layers of water molecules are adsorbed to the solid substrate. However, the thickness of the layer and the vapour phase are an important

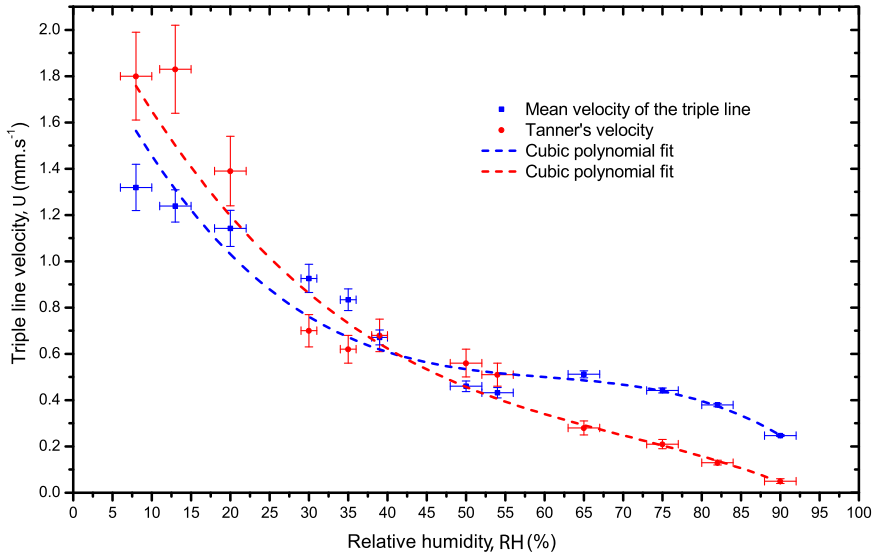

Fig. 10. Mean velocity of the triple line as a function of the RH values. The blue dashed line is the cubic polynomial fit of the mean velocity [$\overline{U} = a + bxRH + cxRH^2 + dxRH^3$ with $a = 2.0$, $b = -7.3 \times 10^{-2}$, $c = 1.17 \times 10^{-3}$, $d = -6.5 \times 10^{-6}$ and $R^2 = 0.94$], passing by the measurements points. The red dashed line is the polynomial cubic fit for tanner's model. (For interpretation of the references to colour in this figure legend, the reader is referred to the web version of the article.)

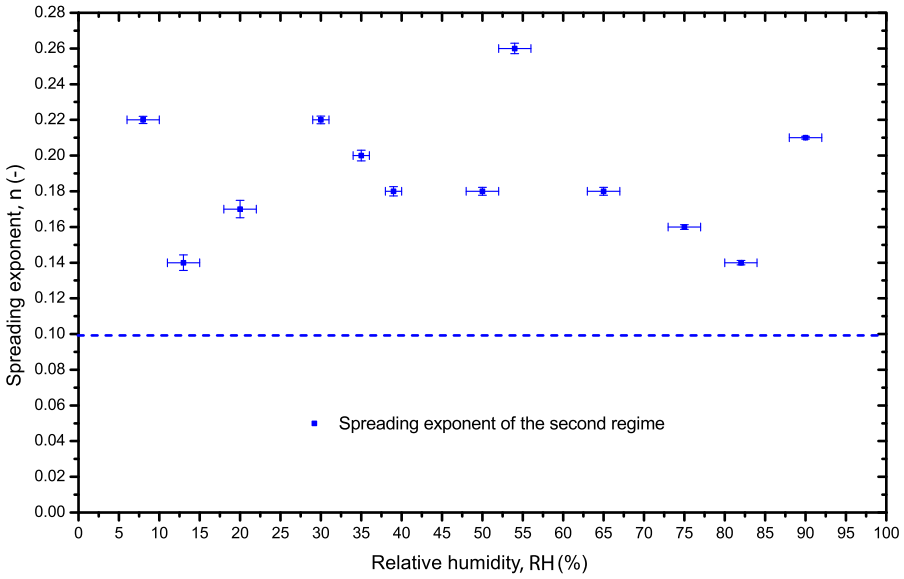

Fig. 11. Spreading exponent of the second regime of spreading (mean value $\overline{n} = 0.19 \pm 0.04$) compared to the spreading exponent of Tanner's model ($n = 0.10$) as a function of the RH.

factors that affects the disjoining pressure. Considerations of these factors was carried out by Starov and Velarde [44].

6. Conclusions and perspectives

The effect of relative humidity on the dynamics of drop spreading on a clean glass surfaces was investigated. Drops of human blood of same volume were allowed to spread on an ultra-clean glass inside a humidity chamber with a controlled RH ranging from 8% to 90%. Our experiments show that the evolution of the wetted area is governed by two distinct regimes. The first is controlled by a viscous-capillary balance with a fast dynamics, whereas the second regime is characterised by much slower dynamics and controlled by a viscous-evaporation rate balance. At early stages of fast spreading, the spreading power law growth as $t^{0.65}$ for different humidities. At late stages of spreading, the exponent of the power law was found to be higher than the exponent of Tanner's law because of the effect of humidity and Marangoni stresses. The spreading dynamics and spreading time were also found to depend on the relative humidity. This is explained by the adhesion of red blood cells to the substrate, which is similar to the mechanism observed for nanofluid droplets. The mean velocity of the triple line was found to follow the same behaviour as Tanner's model, where the final wetting base radius and the apparent contact angle are functions of relative humidity. To optimize our experimental results of velocity, an instantaneous velocity could be used with 5 or 10 points average for each relative humidity.

Acknowledgements

We thank Jerome Vicente for fruitful discussions in image analysis. We thanks also "Carnot Star" Institute (Grant NPC 2012) for their financial support.

References

[1] W.M. Grissom, F.A. Wierum, Spray cooling of a heated surface, Heat Mass Transfer 24 (1981) 261–271.
[2] D. Attinger, Z. Zhao, D. Poulikakos, Experimental study of molten micro-droplet surface deposition and solidification: transient behavior and wetting angle dynamics, Heat Mass Transfer 122 (2000) 544–546.
[3] J. Jing, J. Reed, J. Huang, X. Hu, V. Clarke, J. Edington, D. Housman, T. Anantharaman, E. Huff, B. Mishra, B. Porter, A. Shenker, E. Wolfson, C. Hiort, R. Kantor, C. Aston, D. Schwartz, Automated high resolution optical mapping using arrayed, fluid-fixed DNA molecules, Proc. Natl. Acad. Sci. U.S.A. 95 (1998) 8046–8051.
[4] C. Maier, S. Wiesche, E.P. Hofer, Impact of microdrops on solid surfaces for DNA synthesis, in: Proceedings of the 2000 International Conference on Modeling and Simulation of Microsystems, 2000, pp. 586–589.
[5] O. Voinov, Hydrodynamics of wetting, Fluid Dyn. 11 (1976) 714.
[6] L. Tanner, The spreading of silicone oil drops on horizontal surfaces, J. Phys. D: Appl. Phys. 12 (1979) 1473–1484.
[7] L. Hocking, A. Rivers, The spreading of a drop by capillary action, J. Fluid Mech. 121 (1982) 425–442.
[8] P. de Gennes, Statics and dynamics, Rev. Mod. Phys. 57 (1985) 827.
[9] E. Dussan, E. Rame, S. Garoff, On identifying the appropriate boundary conditions at a moving contact line: an experimental investigation, J. Fluid Mech. 230 (1991) 97–116.
[10] R. Cox, The dynamics of the spreading of liquids on a solid surfaces. Part 1: Viscous flow, J. Fluid Mech. 168 (1986) 169.
[11] A. Carre, F. Eustache, Spreading kinetics of shear-thinning fluids in wetting and dewetting modes, Heat Mass Transfer 16 (2000) 2936–2940.
[12] S. Rafai, D. Bonn, A. Boudaoud, Spreading of non-Newtonian fluids on hydrophilic surfaces, J. Fluid Mech. 513 (2004) 77–85.
[13] D. Bonn, J. Meunier, Viscoelastic free-boundary problems: non-Newtonian viscosity vs normal stress effects, Phys. Rev. Lett. 79 (1997) 14.
[14] J. Lopez, C.A. Miller, E. Ruckenstein, Spreading kinetics of liquid-drops on solids, J. Colloid Interface Sci. 56 (1976) 460–468.
[15] K.G. Winkels, J.H. Weijs, A. Eddi, J.H. Snoeijer, Initial spreading of low-viscosity drops on partially wetting surfaces, Phys. Rev. E 85 (2012) 055301.
[16] J.C. Bird, S. Mandre, Short-time dynamics of partial wetting, Phys. Rev. Lett. 100 (2008) 234501.
[17] A. Eddi, K.G. Winkels, J.H. Snoeijer, Short time dynamics of viscous drop spreading, Phys. Fluids 25 (2013) 013102.
[18] A. Carlson, G. Bellani, G. Amberg, Universality in dynamic wetting dominated by contact line friction, Phys. Rev. E 85 (2012) 045302.
[19] D. Legendre, M. Maglio, Numerical simulation of spreading drops, Colloids Surf. A 432 (2013) 29–37.
[20] A. Biance, C. Clanet, D. Qur, First steps in the spreading of a liquid droplet, Phys. Rev. E 69 (2004) 016301.
[21] V. Chhasatia, A. Joshi, Y. Sun, Effect of relative humidity on contact angle and particle deposition morphology of an evaporating colloidal drop, Appl. Phys. Lett. 97 (2010) 231909.
[22] C. Huh, L. Scriven, Hydrodynamic model of steady movement of a solid/liquid/fluid contact line, J. Colloid Interface Sci. 35 (1971) 85–101.
[23] S. Rafai, D. Bonn, Spreading of non-Newtonian fluids and surfactant solutions on solid surfaces, Physics A 358 (2005) 58–67.
[24] S. Rafai, D. Sarker, V. Bergeron, J. Meunier, D. Bonn, Superspreading: aqueous surfactant drops spreading on hydrophobic surfaces, Langmuir 18 (2002) 10486–10488.
[25] T. Roques-Carmes, V. Mathieu, A. Gigante, Experimental contribution to the understanding of the dynamics of spreading of Newtonian fluids: effect of volume, viscosity and surfactant, J. Colloid Interface Sci. 344 (2013) 180–197.
[26] D. Brutin, B. Sobac, S.J. Loquet B., Pattern formation in drying drops of blood, J. Fluid Mech. 667 (2011) 85–95.

[27] S. Chien, Shear dependence of effective cell volume as a determinant of blood viscosity, Science 168 (1970) 977–978.
[28] P. Easthope, D. Brooks, A comparison of rheological constitutive functions for whole human blood, Biorheology 17 (1980) 235–247.
[29] Y. Cinar, N. Koshu, Hypothesis: temperature stress and blood viscosity affects the leukocyte exibility, coagulation, intracranial hypertension, and hemodynamics, in: IPCBEE, vol. 3, 2011.
[30] Y. Tarasevich, D. Pravoslavnova, Segregation in desiccated sessile drops of biological fluids, Eur. Phys. J. E 22 (2007) 311–314.
[31] D. Bonn, J. Eggers, J. Indekeu, J. Meunier, E. Rolley, Wetting and spreading, Rev. Mod. Phys. 81 (2009) 739–805.
[32] B. Sobac, D. Brutin, Structural and evaporative evolutions in desiccating sessile, Phys. Rev. E 84 (2011) 011603.
[33] D. Brutin, Influence of relative humidity and nano-particle concentration on pattern formation and evaporation rate of pinned drying drops of nanofluids, Colloids Surf. A 429 (2013) 112–120.
[34] W. Bou-Zeid, D. Brutin, Influence of relative humidity on spreading, pattern formation and adhesion of a drying drop of whole blood, Colloids Surf. A 430 (1) (2013) 1–7.
[35] W. Bou-Zeid, J. Vicente, D. Brutin, Influence of evaporation rate on cracks formation of a drying drop of whole blood, Colloids Surf. A 432 (2) (2013) 139–146.
[36] H. Hu, R.G. Larson, Evaporation of a sessile droplet on a substrate, J. Phys. Chem. B 106 (2002) 1334–1344.
[37] R. Deegan, O. Bakajin, T. Dupont, G. Huber, S. Nagel, T. Witten, Capillary flow as the cause of ring stains from dried liquid drops, Nature 389 (1997) 827–828.
[38] H. Hu, R.G. Larson, Analysis of the microfluid flow in an evaporating sessile droplet, Langmuir 21 (2005) 3963–3971.
[39] H. Gelderblom, O. Bloemen, J. Snoeijer, Stokes flow near the contact line of an evaporating drop, J. Fluid Mech. 12 (2012) 1–16.
[40] H. Bodiguel, F. Doumenc, B. Guerrier, Stick-slip patterning at low capillary numbers for an evaporating colloidal suspension, Langmuir 13 (2010) 10758–10763.
[41] A. Cazabat, M. Cohen Stuart, Dynamique de l'etalement de gouttes sur une surface. loi de tanner et effet de la gravite, C. R. Acad. Sci. Paris II 301 (1986) 1337–1339.
[42] S. Zhu, W. Miller, L. Scriven, H. Davis, Superspreading of water-silicone surfactant on hydrophobic surfaces, Colloids Surf. 90 (1994) 63–78.
[43] A. Nikolov, D. Wasan, A. Chengara, K. Koczo, G. Policello, I. Kolossvary, Superspreading driven by Marangoni flow, Adv. Colloid Interface Sci. 96 (2002) 325–338.
[44] V.M. Starov, M.G. Velarde, Surface forces and wetting phenomena, J. Phys.: Condens. Matter 21 (2009) 464121.
[45] E.Y. Bormashenko, Wetting of Real Surfaces, De Gruyter, Paris, 2013.